Geophysical Research Letters

Mesospheric Q2DW Interactions With Four Migrating Tides at 53°N Latitude: Zonal Wavenumber Identification Through Dual-Station Approaches

Maosheng He[1] , Jeffrey M. Forbes[2] , Guozhu Li[3,4] , Christoph Jacobi[5] , and Peter Hoffmann[1,†]

[1]Leibniz-Institute of Atmospheric Physics at the Rostock University, Kühlungsborn, Germany, [2]Ann & H.J. Smead Department of Aerospace Engineering Sciences, University of Colorado, Boulder, CO, USA, [3]Beijing National Observatory of Space Environment, Institute of Geology and Geophysics, Chinese Academy of Sciences, Beijing, China, [4]College of Earth and Planetary Sciences, University of Chinese Academy of Sciences, Beijing, China, [5]Institute for Meteorology, Universitaet Leipzig, Leipzig, Germany

Abstract Mesospheric winds from two longitudinal sectors at 53°N latitude are combined to investigate quasi-two-day waves (Q2DWs) and their nonlinear interactions with tides. In a summer 2019 case study, we diagnose the zonal wavenumber m of spectral peaks at expected frequencies through two dual-station approaches, a phase differencing technique (PDT) on individual spectral peaks and a least squares procedure on family batched peaks. Consistent results from the approaches verify the occurrences of Rossby-gravity modes ($m = 3$ and 4 at periods $T = 2.1$ and 1.7 days), and their secondary waves (SWs) generated from interactions with diurnal, semi-diurnal, ter-diurnal, and quatra-diurnal migrating tides. We further extend the PDT to 2012–2019, illustrating that Q2DWs exhibit significant interannual variability. Composite analysis reveals seasonal and altitude variations of the Rossby-gravity modes and their SWs. The Rossby-gravity modes maximize in local summer, whereas their 16- and 9.6-h SWs appear more in winter.

Plain Language Summary The quasi-two-day wave is the strongest and most widely studied planetary wave occurring in the mesosphere. Existing observational analyses are based on either single-satellite or -station approaches, which suffer from temporal and spatial aliasing, respectively. The current study implements and develops dual-station approaches to investigate the mesospheric quasi-two-day wave at 53°N latitude, in a case and a statistical study. Our approaches allow diagnosing both the frequency and zonal wavenumber. In the case study, we diagnosed two Rossby-gravity modes and the secondary waves (SWs) of the nonlinear interactions between the Rossby-gravity modes and the migrating tides at periods of 24, 12, 8, and 6 h. While the interactions with the 24- and 12-h tides are expected, those with the 8- and 6-h tides are reported for the first time. In the statistical study, we report the seasonality and altitude variation of the Rossby-gravity modes and their most dominant SWs.

1. Introduction

The quasi-two-day wave (Q2DW) is perhaps the largest and most widely studied planetary wave (PW) in the mesosphere. Tunbridge et al. (2011) gave an excellent historical account of observational and theoretical studies on the Q2DW. Briefly, the Q2DW was first discovered in meteor radar winds (Babadshanov et al., 1973; Muller, 1972) and was later proposed theoretically to be the atmospheric manifestation of the gravest westward-propagating normal mode with zonal wavenumber $m = 3$ (e.g., Salby, 1981). Alternatively, the Q2DW is explained as the response to instability in the mesospheric summer westward jet, with potential zonal wavenumbers $m = 2$–4 (Pfister, 1985; Plumb, 1983). The Q2DW seems like a near-resonant oscillation excited and/or amplified by an instability (Randel, 1994). Within the satellite era, various space-based observations have been explored to study the Q2DW (Huang et al., 2013; Moudden & Forbes, 2014; Pancheva et al., 2018), delineating seasonal-latitudinal and interannual variabilities of Q2DWs with $m = 2$–4 (cf., Tunbridge et al., 2011). Insightful analyses on the Q2DW have also been performed using a global middle atmosphere assimilation model (Lieberman et al., 2017; Pancheva et al., 2016).

An intriguing aspect of the early radar studies was the discovery (e.g., Manson et al., 1982) that nonlinear interaction between the Q2DW, and the semi-diurnal tide yields 9.6- and 16-h secondary waves (SWs) which are sometimes observed in the wind spectra (Beard et al., 1999; Cevolani & Kingsley, 1992). The underlying theory was further developed (Teitelbaum et al., 1989; Teitelbaum & Vial, 1991) to include longitude dependence of the waves, tide-tide and -PW interactions. The interactions are regulated by the resonance conditions (RCs, e.g., He et al., 2017; Teitelbaum & Vial, 1991). Assume that at longitude λ and time t, the disturbance, induced by a zonal traveling wave with an amplitude $\tilde{\alpha}$ and zonal wavenumber m at frequency f, could be represented as,

$$\tilde{\Psi}\left(\lambda,t \mid f,m\right) := \tilde{\alpha}\tilde{\psi}\left(\lambda,t \mid f,m\right) := \tilde{\alpha}e^{i\left(2\pi ft+m\lambda\right)} \tag{1}$$

Then, two waves, $\tilde{\alpha}_1\tilde{\psi}_1(\lambda,t \mid f_1,m_1)$ and $\tilde{\alpha}_2\tilde{\psi}_2(\lambda,t \mid f_2,m_2)$, might interact nonlinearly and generate an SW, $\tilde{\alpha}_{SW}\tilde{\psi}_{SW}(\lambda,t \mid f_{SW},m_{SW})$. The RCs specify,

$$\tilde{\psi}_{SW} = \tilde{\psi}_1\tilde{\psi}_2, \tilde{\psi}_1\tilde{\psi}_2^*, \tilde{\psi}_1^*\tilde{\psi}_2, \text{or}, \tilde{\psi}_1^*\tilde{\psi}_2^* \tag{2}$$

hereafter, $\tilde{\bullet}^*$, $\Re(\tilde{\bullet})$, and $\arg\{\tilde{\bullet}\}$ denote the conjugate, real part, and argument (in the range $0-2\pi$ excluding 2π) of a complex value $\tilde{\bullet}$, respectively. Since $\Re\left(\tilde{\psi}_1\tilde{\psi}_2^*\right) = \Re\left(\tilde{\psi}_1^*\tilde{\psi}_2\right)$, $\tilde{\psi}_1\tilde{\psi}_2^*$ and $\tilde{\psi}_1^*\tilde{\psi}_2$ represent the same wave, and so do $\tilde{\psi}_1^*\tilde{\psi}_2^*$ and $\tilde{\psi}_1\tilde{\psi}_2$. Therefore, only two SWs in Equation 2 are independent: $\Re\left(\tilde{\psi}_1\tilde{\psi}_2\right)$ and $\Re\left(\tilde{\psi}_1\tilde{\psi}_2^*\right)$, termed, hereafter, as upper and lower sidebands (USB and LSB), respectively.

Equation 2 implies,

$$f_{SW} = f_1 \pm f_2, \text{and}, m_{SW} = m_1 \pm m_2 \tag{3}$$

According to Equation 3, the interactions between the Rossby-gravity (R-G) modes (Q2DWs with $m = 3$ and 4, Q2DW3 and Q2DW4) and the diurnal and semi-diurnal migrating tides (DW1 and SW2, at $f = 1$ and 2 cpd with $m = 1$ and 2, respectively) could generate up to eight SWs. The SWs populate at three periods, 2 days, 16 h, and 9.6 h with different m, as sketched in the f-m depiction in Figure S1a. In addition, these three periods are also populated by SWs of interactions between Q2DWs and various non-migrating tides (Forbes & Moudden, 2012).

The importance of Q2DW-tide interactions to atmosphere-ionosphere coupling was recently demonstrated using a whole-atmosphere-ionosphere general circulation model (e.g., Gu et al., 2018). Although the cross-mesopause propagations of Q2DWs are subject to background winds (Salby & Callaghan, 2001), a subset of their SWs can propagate well into the E-region (Nguyen et al., 2016; Palo et al., 1999) and generate electric fields that carry the Q2DW periodicity to the F-region (Gu et al., 2018). The point here is that eastward- (westward-) propagating waves favor propagation into regions of prevailing westward (eastward) zonal-mean winds. The presence of SWs in the wind spectrum is significant, since they propagate freely as independent oscillations and contribute measurably to the longitude-time structure and complexity of the overall dynamics (e.g., Pedatella & Forbes, 2012) and to the ionospheric response (Gu et al., 2018). A major challenge to date has been our inability to unequivocally determine which 9.6- and 16-h waves are present in the atmosphere at any given time. As noted above, while ground-based observations allow identifying the SWs at expected frequencies, they provide no information on the wavenumber m. From the vantage point of a slowly precessing satellite, a wave X, at f_X with m_X in Earth-fixed coordinate system O, appears at its Doppler-shifted frequency $f_X' = \left|m_X - \dfrac{f_X}{1\text{cpd}}\right| * 1\text{cpd}$ in the sun-synchronous coordinate system O'. Specially, all migrating tides ($m = \dfrac{f}{1\text{cpd}}$) are shifted to $f' = 0$, and their interactions with X generate SWs at also f_X' according to the RCs (Equation 3). Therefore, X and all the SWs cannot be distinguished from each other. On this ambiguity, there are equivalent explanations implementing the RCs in O and inspecting the waves in either O or O' (e.g., Forbes & Moudden, 2012; He et al., 2011; Nguyen, et al., 2016). In O, the quantity $\dfrac{f_X'}{1\text{cpd}} = \left|m_X - \dfrac{f_X}{1\text{cpd}}\right|$ is also discussed as the apparent or spaced-based zonal wavenumber. Forbes

and Moudden ([2012](#)) specified the apparent wavenumbers of SWs of the Q2DW interactions with various migrating and non-migrating tides.

In summary, single-satellite or -station approaches suffer from temporal and spatial aliasing (Text S1, He, Chau, et al., [2020](#)), respectively. In the present paper, we use two dual-station approaches, one developed here and the other developed in He et al. ([2018](#)), to identify f and m of diverse SWs arising from Q2DW-tide interactions.

2. Data Analysis

Following the single-wave assumption (He, Chau, et al., [2020](#), and references therein), we assume that at f there exists only one wave traveling zonally, denoted as $\tilde{\Psi} = \tilde{a}(\lambda)e^{i2\pi ft}$ where $\tilde{a}(\lambda) := \tilde{\alpha}e^{im\lambda}$ according to Equation [1](#). $\tilde{a}(\lambda)$ could be estimated spectrally using observations collected at two longitudes, denoted as $\tilde{a}(\lambda_1)$ and $\tilde{a}(\lambda_2)$. Their cross product,

$$\tilde{c} := \tilde{a}(\lambda_1)\tilde{a}^*(\lambda_2) = |\tilde{\alpha}|^2 e^{im(\lambda_1 - \lambda_2)} := |\tilde{\alpha}|^2 e^{im\lambda_\Delta} \tag{4}$$

allows estimating m,

$$m = \frac{\arg\{\tilde{c}\} + 2Z\pi}{\lambda_\Delta} = \frac{\arg\{\tilde{c}\}}{\lambda_\Delta} + \frac{2\pi Z}{\lambda_\Delta} := m_0 + Z\Delta_m \tag{5}$$

here, $\arg\{\tilde{c}\} + 2\pi Z$ represents the phase difference between the longitudes, where $Z \in \mathbb{Z}$ is an integer representing a whole-cycle ambiguity. All possible m values are aliases of m_0, and Δ_m denotes the Nyquist sampling theorem in the spatial domain. This approach is called the phase differencing technique (PDT; He et al., [2018](#)). In Sections [3](#) and [4](#), we implement and develop the PDT in a case and statistical study, respectively.

We use meteor radar winds over two sites, Mohe (M, 122°E, 54°N) and northern Germany (G, 13°E, 53°N). The Mohe radar was introduced in Yu et al. ([2013](#)), whereas at Germany echoes from two radars, at Juliusruh (13°E, 55°N; Hoffmann et al., [2010](#)) and Collm (13°E, 51°N; Jacobi, [2012](#); Lilienthal & Jacobi, [2015](#)), are used to expand the temporal coverage. Hourly zonal and meridional winds (u and v) are estimated on an altitude grid $h = 80.5, 81.5,..., 99.5$ km through the approach in Hocking et al. ([2001](#)).

3. A Case Study

The winds, u and v, at Mohe and Germany between June 1 and September 15, 2019, are used to calculate the Lomb-Scargle spectra, yielding complex amplitudes $\tilde{a}_u^M, \tilde{a}_v^M, \tilde{a}_u^G$, and $\tilde{a}_v^G$, at each altitude. The amplitudes are used to calculate $\left\langle \left| \tilde{a}_u^2 \right| + \left| \tilde{a}_v^2 \right| \right\rangle$, averaged between G and M. As displayed in Figure [1a](#), $\left\langle \left| \tilde{a}_u^2 \right| + \left| \tilde{a}_v^2 \right| \right\rangle$ at $h > 96$ km is noisy, potentially due to the relatively low density of meteor count (Chau & Clahsen, [2019](#)). Therefore, the current work focuses mainly on $h < 96$ km. To implement Equation [4](#), we calculate the cross product $\tilde{c}_u := \tilde{a}_u^{M*}\tilde{a}_u^G$ and $\tilde{c}_v := \tilde{a}_v^{M*}\tilde{a}_v^G$, and then the altitude average $\tilde{c} := \langle \tilde{c}_u + \tilde{c}_v \rangle_{80<h<96\text{km}}$ displayed in Figure [1b](#). To inspect the details in Figure [1b](#), we develop a representation in Section [3.1](#), with which we estimate m of spectral peaks using two approaches. The results are summarized in Figure [S1b](#) and Table [1](#) and explained below.

3.1. Spectral Periodic Table

We divide the $\tilde{c}(f)$ spectrum in Figure [1b](#) into 0.5-cpd-wide segments, as denoted by the color bars on top of Figure [1b](#), indexed as $N\pm$, that is, 0+,1−,1+,...,3+. $N\pm$ segment comprises f between N and $N \pm 0.5$ cpd. Each segment is zoomed into one row in Figure [1c](#) and arranged according to $|\delta f| := \left| f - \lfloor f \rceil \right|$, namely, the distance between f and its nearest integer $\lfloor f \rceil$ (hereafter, for simplicity, we use f to denote $\frac{f}{1\text{cpd}}$, namely, the value in the unit of cpd). We name the representation of Figure [1c](#) as the spectral periodic table (SPT).
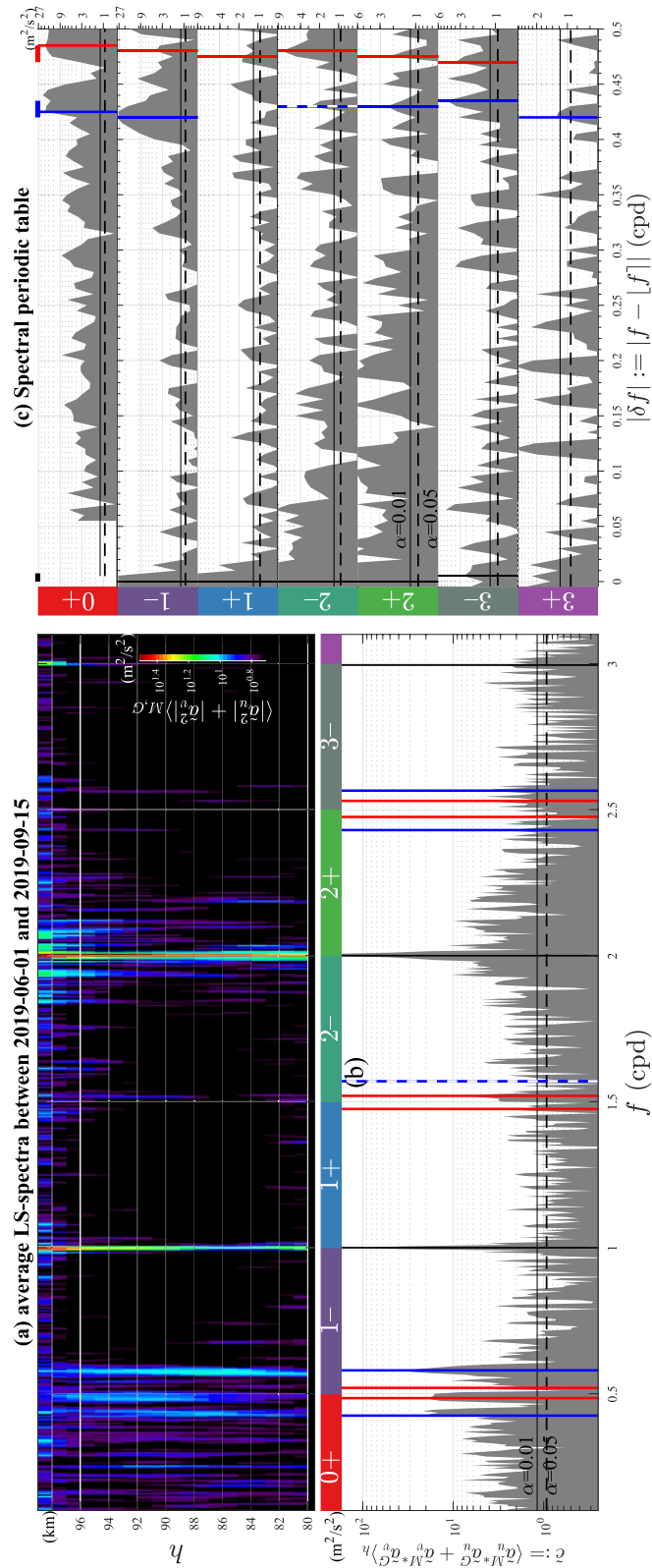
Figure 1. (a) Lomb-Scargle spectra $\langle|\tilde{a}_u^2|+|\tilde{a}_v^2|\rangle_{M,G}$, averaged between the two longitudes, Mohe and Germany, (b) altitude average of the cross-spectrum $\tilde{c} := \langle\tilde{a}_u^{M*}\tilde{a}_u^G + \tilde{a}_v^{M*}\tilde{a}_v^G\rangle_h$, and (c) a periodic table representation of (b). (b) is divided into segments denoted by the color bars on top of the panel and labeled as "0+," "1−," "1−," .... Each of the segments is zoomed in and displayed in (c) as one row labeled on the very left. In (c), the x-axis represents $|\delta f| := |f - \lfloor f\rceil|$, namely, the distance between f and its nearest integer $\lfloor f\rceil$. In (b), (c), the horizontal black lines denote significance levels $\alpha = 0.01$ and 0.05; the vertical blue, red, and black lines indicate three families of spectral peaks. Peaks from the same family share the same $|\delta f|$ value and are used to diagnose the m through two approaches and specified in Table 1. Diagnoses from the two approaches are consistent at some peaks but inconsistent at the others, denoted by the solid and dashed lines, respectively. The white horizontal white lines in (a) indicate the spectrum used for calculating (b). See Section 3 for details.

Table 1
Wavenumber Estimation Through Two Approaches: m^{PDT} versus m^F

$N\pm$	f (cpd)	T (hr)	$\sqrt{|\tilde{c}|}$ (m/s)	m^{PDT}	m^F	δm (Eq. 9)	$m^{PDT} \approx m^F$ ($\delta m < 0.5$)	potential wave[a]
1±	1.000	24.0	9.3	0.95+3.31Z	1	0.05	✓	24hr migrating tide (DW1)
2±	2.000	12.0	20.6	1.89+3.31Z	2	0.11	✓	12hr migrating tide (SW2)
3±	2.995	8.0	1.6	0.15+3.31Z	3	0.46	✓	8hr migrating tide (TW3)
4±	4.000	6.0	1.1	0.25+3.31Z	4	0.44	✓	6hr migrating tide (QW4)
0+	0.425	56.5	4.3	0.54+3.31Z	−3	0.23	✓	DW1–Q2DW4[b]
1−	0.580	41.4	5.5	1.14+3.31Z	4	0.45	✓	Q2DW4[b]
2−	1.570	15.3	1.7	2.65+3.31Z	5	0.96	×	DW1+Q2DW4[c]
2+	2.430	9.9	1.5	2.57+3.31Z	−1	0.26	✓	TW3–Q2DW4[d]
3−	2.565	9.4	2.1	2.74+3.31Z	6	0.05	✓	SW2+Q2DW4[d]
3+	3.420	7.0	1.1	0.25+3.31Z	0	0.25	✓	QW4–Q2DW4
0+	0.485	49.5	4.4	2.72+3.31Z	3	0.28	✓	Q2DW3[b]
1−	0.520	46.2	2.0	0.93+3.31Z	−2	0.38	✓	DW1–Q2DW3[b,e]
1+	1.475	16.3	1.3	1.00+3.31Z	4	0.31	✓	DW1+Q2DW3[c,f]
2−	1.520	15.8	2.8	2.55+3.31Z	−1	0.25	✓	SW2–Q2DW3[c]
2+	2.475	9.7	1.5	1.57+3.31Z	5	0.12	✓	SW2+Q2DW3[d]
3−	2.530	9.5	1.9	0.34+3.31Z	0	0.34	✓	TW3–Q2DW3[d]

[a]In the last column, the symbols "−" and "+" represent the LSB- and USB-generating interactions between the waves at the flanks of the symbols, respectively. [b]Collectively referred to as near-2-day waves. [c]Collectively referred to as near-16-h waves. [d]Collectively referred to as near-9.6-h waves. [e]Also known as Q2DE2. [f]Can also be explained as SW2-Q2DE2 interaction.

The RCs (Equation 3) specify the frequency relations between SWs, and their parent waves: $f_{SW} = f_1 \pm f_2$. Specially, when $\left|f_1 - \lfloor f_1 \rceil\right| = 0$ (namely, $f_1 = 1, 2, 3, \ldots$ cpd), $\left|f_{SW} - \lfloor f_{SW} \rceil\right| \equiv \left|f_2 - \lfloor f_2 \rceil\right|$, revealing that in the SPT all potential SWs of interactions between tides and any wave at f_2 locate at the column comprising f_2.

On top of the SPT (Figure 1c), there are short horizontal bars in black, blue, and red, corresponding to the three maximum peaks of $P\left(\left|\delta f\right|\right) := \prod_{N\pm} \left|\tilde{c}\left(\left|\delta f\right|\right)\right|$. Each of these bars represents a 0.015-cpd-wide δf interval, narrower than the spectral frequency resolution $2\sigma_f \sim 2/T_w = 2/106\text{d} = 0.019$ cpd. Here $T_w = 106$ d is the window width. For example, the black bar corresponds to $\delta f = 0 \pm 0.0075$ cpd. The following three subsections deal with these intervals, respectively.

3.2. The Tidal Signatures

At $\delta f = 0 \pm 0.0075$ cpd in each row of Figure 1c, we search for a maximum spectral peak, displayed as the vertical black lines in Figures 1b and 1c and specified in black in Table 1. The $\tilde{c}$ values at these maximum peaks are substituted in Equation 5, resulting in the PDT estimations m^{PDT} listed in Table 1. Note that m^{PDT} comprises aliases denoted by $Z\Delta_m$, where $\Delta_m = 3.31$ is determined by our radar separation. At $f = 1.0, 2.0, 3.0,$ and 4.0 cpd, $m^{PDT} = 0.95, 1.89, 3.46,$ and 3.56, when $Z = 0, 0, 1,$ and 1, respectively. The nearest integers of m^{PDT} are $\lfloor m^{PDT} \rceil = 1, 2, 3,$ and 4, as listed in the column m^F in Table 1. Therefore, we explain the corresponding spectral peaks as migrating solar tides, DW1 SW2, TW3, and QW4 (diurnal, and semi-, ter-, and quatra-diurnal westward traveling tides with $m = 1, 2, 3,$ and 4).

3.3. The Q2DW4 Family

Similarly, at $\left|\delta f\right| = 0.4275 \pm 0.0075$ cpd, denoted by the blue bar on top of Figure 1c, we search for the maximum peak in each row of Figure 1c, above the significance level $\alpha = 0.01$. Six maxima are searched and displayed as the vertical blue lines in Figures 1b and 1c, whose frequencies and $\tilde{c}$ values (denoted as $\tilde{c}_{N\pm}$) are specified in blue in Table 1. Substituting $\tilde{c}_{N\pm}$ for $\tilde{c}$ in Equation 5 results in the PDT estimations $m^{PDT}_{N\pm}$ specified in Table 1. To deal with the ambiguities represented by Z in $m^{PDT}_{N\pm}$, below we present a family batched estimation of $m_{N\pm}$.

According to Equation 4,

$$\tilde{c}_{N\pm} \, / \, \left| \tilde{c}_{N\pm} \right| = e^{im_{N\pm}\lambda_{\Delta}} \tag{6}$$

here, $m_{N\pm}$ might not be completely independent but regulated by the RCs (Equation 3), if underlying waves generate each other by interacting nonlinearly with the tides identified in Section 3.2. In the most extreme case, only one wave is independent and all the others are associated SWs. In this single-independent-wave case, only one wavenumber is independent, and $m_{N\pm}$ can be represented as:

$$m_{N\pm} = N \pm m_{0+} \tag{7}$$

Substitute $m_{N\pm}$ in Equation 6,

$$\tilde{c}_{N\pm} \, / \, \left| \tilde{c}_{N\pm} \right| = e^{i(N\pm m_{0+})\lambda_{\Delta}} \; \Rightarrow \; e^{-iN\lambda_{\Delta}} \tilde{c}_{N\pm} \, / \, \left| \tilde{c}_{N\pm} \right| = e^{\pm im_{0+}\lambda_{\Delta}} \tag{8}$$

which is an overdetermined system comprised of only one unknown m_{0+} and six equations. We first estimate the least squares solution of $e^{im_{0+}}$ denoted as $\tilde{e}_{LS}$, and then estimate m_{0+} through an optimization $m_{0+}^{F} = \underset{\hat{m}}{\operatorname{argmax}} \, \Re\left(\tilde{e}_{LS}^{*} e^{i\hat{m}} \right)$, subject to: $\hat{m} \in \left[-5, -4, \ldots, 5 \right]$. Here, we use the superscript F to distinguish the family batched estimations $m_{N\pm}^{F}$ from the PDT estimations $m_{N\pm}^{PDT}$.

Solving the optimization yields the estimation $m_{0+}^{F} = -3$. Other $m_{N\pm}^{F}$ are calculated according to Equation 7, listed in blue in the column m^{F} in Table 1 and compared with $m_{N\pm}^{PDT}$. The comparison results are listed in the column $m^{F} \approx m^{PDT}$ in Table 1, in which checkmarks "✓" denote consistencies between $m_{N\pm}^{F}$ and $m_{N\pm}^{PDT}$ whereas the cross mark "✕" denotes an inconsistency. The consistency is claimed if $\exists Z : \lfloor m_{N\pm}^{PDT}(Z) \rceil = m_{N\pm}^{F}$ which equals to,

$$\delta m_{N\pm} := \min \left| m_{N\pm}^{PDT} - m_{N\pm}^{F} \right| < 0.5 \tag{9}$$

Among the six estimations, five estimations exhibit consistency, among which the one at $f = 0.58$ cpd could be explained as the R-G mode Q2DW4 (e.g., Salby & Callaghan, 2001). Accordingly, we explain the remaining four as the SWs of tide ±Q2DW4 interactions specified in the last column in Table 1. (Here, + and – represent the USB- and LSB-generating interactions, respectively.) The blue symbols in Figure S1b present the five consistent estimations in the f-m plane.

The above SPT analysis utilizes the constraints of the RCs of f and m. Conventionally, the single-station bispectral analysis is used to explore nonlinear interactions, exploiting the constraints of the RC of f and quadratic phase coupling relations (e.g., Beard et al., 1999). We also produce a bispectrum using our Lomb-Scargle spectra (Figure S2). While each of the interactions suggested in Table 1 is associated with a bispectral peak, some of the bispectral peaks are absent in Table 1. For example, the peak indicated by the blue arrow in Figure S2e suggests the DW1+Q2DW interaction, which is absent in Table 1.

3.4. The Q2DW3 Family

Further, we implement the above peak identification, least squares estimation, and optimization, at $\left| \delta f \right| = 0.4775 \pm 0.0075$ cpd denoted by the red bar on top of Figure 1c. The results are displayed as the vertical red lines in Figures 1b and 1c and specified in red in Table 1. The family batched estimation m^{F} and the individual PDT estimation m^{PDT} are consistent for all six peaks, denoted as the red symbols in Figure S1b. Among the six peaks, the one at $f = 0.485$ cpd is explained as the Q2DW R-G mode with $m^{F} = 3$ (Q2DW3, e.g., Salby & Roper, 1980). Therefore, the remaining five peaks are explained in terms of migrating-tides ±Q2DW3 interactions specified in the last column in Table 1.
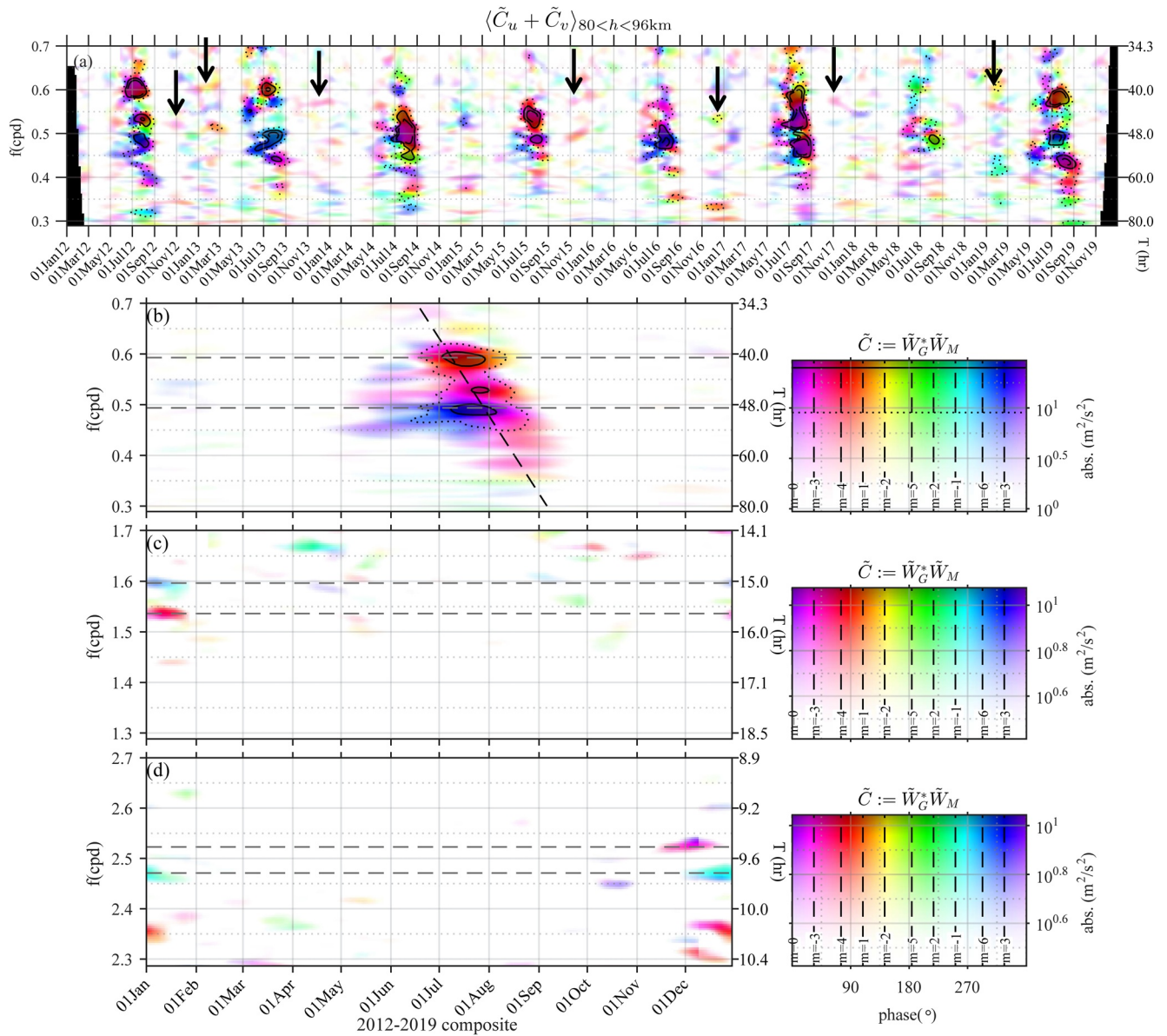
Figure 2. (a) 2012–2019 composited $\langle \tilde{C}_u + \tilde{C}_v \rangle_h$, namely, the sum of the cross-wavelet spectra of u and v wind components between the two longitudes, averaged in the altitude range $80 < h < 96$ km and frequency range $f \in \Delta f := [0.3, 0.7\ \text{cpd}]$. (b) The composite spectrum of (a). (c), (d) same plots as (b) but in the frequency ranges $\Delta f + 1$ and $\Delta f + 2$, respectively. (a) and (b) share the same color-code map, in which the dotted, solid, and dashed black isolines denote amplitudes at $\sqrt{|\tilde{C}|} = 3, 4$, and 5 m/s.

To our knowledge, it is for the first time that TW3 and QW4 are reported interacting nonlinearly with PWs. These results demonstrate clearly that the PW-tide interactions increase the variety of waves in the upper mesosphere and lower thermosphere region, more than was previously known.

4. 2012–2019 Composite Analysis

The previous section implements the PDT in the summer 2019 case using the Lomb-Scargle method. In the current section, we extend the PDT implementation to 8 years (2012–2019) after replacing the Lomb-Scargle method with the cross-wavelet method (He, Chau, et al., 2020). We first calculate the Gabor wavelet (Torrence & Compo, 1998) of u and v components over Germany and Mohe at each altitude h, resulting in

amplitudes $\tilde{W}^{G,u,h}_{(f,t)}, \tilde{W}^{G,v,h}_{(f,t)}, \tilde{W}^{M,u,h}_{(f,t)},$ and $\tilde{W}^{M,v,h}_{(f,t)}$. These amplitudes are the observational estimations of $\tilde{a}(\lambda)$ in Equation 4 and are functions of t and f. Then, the cross product $\tilde{C} := \tilde{W}^{G*}_{(f,t)}\tilde{W}^{M}_{(f,t)}$, namely, the cross-wavelet spectrum, is the observational estimation of $\tilde{c}$ in Equation 4. We sum the cross-wavelet spectra of u and v components, yielding $\tilde{C}_{u+v} := \tilde{C}_u + \tilde{C}_v$. In Sections 4.1 and 4.2, we inspect altitude-averaged $\tilde{C}_{u+v}$ in the f-t depiction and $\tilde{C}_{u+v}$ at discrete frequencies in h-t depiction.

4.1. Altitude-Averaged Cross-Wavelet Spectra

Figure 2a displays $\langle \tilde{C}_{u+v} \rangle_{80<h<96\text{km}}$, in which the darkness represents the magnitude while the color hue denotes its phase. The magnitude exhibits an annual variation, maximizing in local summer (July–September) with dim spectral peaks in local winter.

$\langle \tilde{C}_{u+v} \rangle_h$ is composited as a function of the month, displayed in Figure 2b. As indicated by the black dashed line in Figure 2b, the composite spectrum maximizes largely earlier at a higher frequency. Below, we focus on the frequency range $\Delta f_{Q2DW} := 0.40$–0.60 cpd where the strongest spectral peaks occur. The strongest two peaks are the red one at $f = 0.57$–0.60 cpd ($T = 40.0$–42.1 h) and the blue at $f = 0.48$–0.50 cpd ($T = 48.0$–50.0 h), both of which appear in July. The redness and blueness are associated with $m = 4$ and 3, respectively. These two peaks can be explained as R-G modes Q2DW4 and Q2DW3 because both their f and m are consistent with the theoretical expectations $[T,m] = [1.7$ days$,4]$ and $[2.1$ days$,3]$ (Salby & Callaghan, 2001). Except for the red and blue peaks, Figure 2b is dominated mainly by magenta associated with $m = -3$ (Q2DE3), including a peak at $f = 0.52$–0.55 cpd in July and the smeared region within $f = 0.35$–0.50 cpd in August. The smeared Q2DE3 signature could be explained as the LSB of the interaction between DW1 and Q2DW4 at $f = 0.57$–0.60 cpd, whereas the Q2DE3 peak at $f = 0.52$–0.55 cpd might not be excited in-situ as no Q2DW4 signature appears at the required frequency.

The above four Q2DW signatures exhibit significant interannual variabilities, as revealed in Figure 2a. The Q2DW3 signature occurred in summers of 2012, 2013, 2016, and 2019; the Q2DW4 occurred in 2012, 2013, 2017, and 2019; the Q2DE3 signature at $f = 0.35$–0.50 cpd occurred weakly in 2012, 2014, 2015, 2016, and 2017; and the Q2DE3 signature at $f = 0.50$–0.55 cpd occurred in 2012, 2014, 2015, 2016, and 2017. Besides, at $f = 0.45$–0.55 cpd occurred the green peak in 2012, 2014, 2018, and 2019, which is not visible in the composite spectrum. The greenness suggests $m = 2$ (Tunbridge et al., 2011).

Figures 2c and 2d present the same plots as Figure 2b but for periods near 16 and 9.6 h, namely, frequency ranges of the SWs. Given that in Figure 2b Q2DWs occur mainly within $\Delta f_{Q2DW} := 0.40$–0.60 cpd, we focus hereafter on $\Delta f_{Q2DW} + 1.00$ cpd and $\Delta f_{Q2DW} + 2.00$ cpd. In these ranges, the most dominant two near-16-h and -9.6-h peaks are along the dashed gray line, all occurring during November–January. Similar SW signatures also occur in the summer throughout 2012–2019 in the spectra in Figure S3. The summer signatures are weak and almost saturated out in the composite spectra in Figures 2c and 2d. The winter SWs were also observed in the southern hemisphere (Alves et al., 2013). We discuss this seasonality further in the next subsection.

4.2. Altitude Variation

Figure 3 displays the composite spectra of $\tilde{C}_{u+v}$ as a function of the month and altitude at the frequencies illustrated by the horizontal gray dashed lines in Figures 2b–2d. Figures 3a and 3b capture the Q2DW3 and Q2DW4, respectively. While the Q2DW3 occurs mainly above 90 km, the Q2DW4 peak extends to a lower altitude. Such a difference could be observed in the geopotential amplitudes at southern hemispheric mid-latitude in a theoretical computation (Figures 6 vs. 10; Salby & Callaghan, 2001). The computation suggests that the Q2DW4 is strongly distorted by the mean wind and does not penetrate much across the mesopause whereas the Q2DW3 extends upward into the thermosphere.

In Figure S1, there are four potential near-16-h SWs: $m = -2, -1, 4,$ and 5, and four near-9.6-h: $m = -1,$ 0, 5, and 6. Among the potential near-16-h SWs, the $m = 4$ peak in Figure 3c is stronger than the peak in
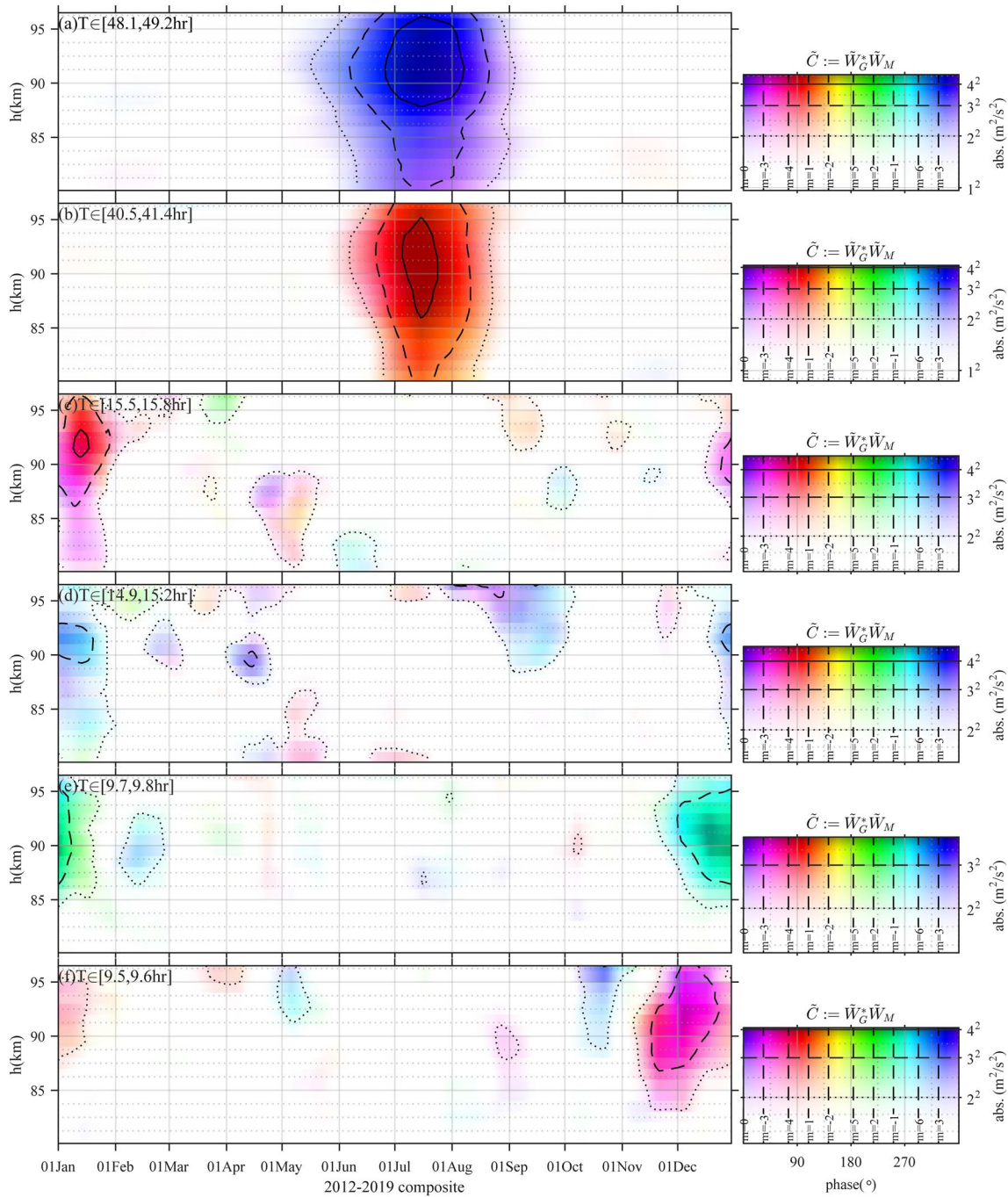
Figure 3. Multi-year composited $\tilde{C}_u + \tilde{C}_v$, as a function of month and altitude at six periods indicated by the horizontal dashed lines in Figures 2b–2d.

Figure 3d. At near-9.6 h, the $m = 0$ amplitude in Figure 3f is comparable to the $m = -1$ in Figure 3e. All the SWs maximize in the local winter, resulted potentially from the seasonality of tides and Q2DWs, as proposed speculatively in the following paragraphs.

According to the Manley-Rowe relation (He et al., 2017), tides contribute more energy than PWs in generating SWs, and therefore might be more important in shaping SWs' seasonality (note that the Manley-Rowe relation deals with the wave mode's global total energy but not the energy spatial distribution, and therefore cannot exactly quantify the local amplitudes of the relevant waves). The dominant tidal component at 53°N is the semi-diurnal (Figure 4 in He, Forbes, et al., 2020), comprising mainly SW2 that maximizes

in December–January (Figure 4k in He & Chau, 2019). Meanwhile, Q2DWs with $m = -2$ and -3 (Q2DE2 and Q2DE3) arise occasionally in the northern hemisphere winter, potentially from the stratospheric jet instability (Merzlyakov et al., 2005; Pancheva et al., 2016; Sandford et al., 2008), mainly below 80 km altitude (Gu et al., 2017; Pancheva et al., 2016). Consistently, in the spectra above 80 km in Figure 1a, the winter Q2DE2 and Q2DE3 signatures, namely, the yellow and magenta peaks indicated by the downward black arrows, are weak and erratic. The vertical propagation (dissipation) of waves is inhibited (enhanced) for slower phase speeds relative to the zonal-mean flow. Accordingly, the prevailing eastward wind in the winter mesosphere disfavors the upward propagation of the Q2DE2 and Q2DE3 more than the $m = -1$ SW, but promotes the propagation of SWs with $m > 0$. Therefore, SW2–Q2DE2 and SW2+Q2DE3 interactions can generate the $m = 4$ and -1 SWs at low altitudes, and the SWs can propagate upward above 80 km, as captured in Figures 2c and 2e. The $m = 0$ peak in Figure 2f is attributable to the TW3–Q2DW3 interaction, since the local ter-diurnal tide maximizes annually in October–December (Figure 4, He, Forbes, et al., 2020).

Another possible explanation for the SWs' seasonality is the annual variation of the southern hemispheric Q2DWs that maximize during December–January (Salby & Callaghan, 2001). The southern hemispheric Q2DW prefers $T = 48$–52 h and $m = 3$ (Tunbridge et al., 2011), whereas the northern hemispheric Q2DW tends to spread out in T and m. Therefore, the southern hemispheric Q2DWs and the associated SWs should be more repeatable from year to year. The SWs might extend to northern hemispheric mid-latitudes and occur in both hemispheres during December–January.

5. Summary

Mesospheric winds, from two longitudinal sectors at 53°N, are combined to investigate the Q2DW in a summer 2019 case study and an 8-year statistical study. In the case study, PDT is first implemented to diagnose zonal wavenumber m of the Lomb-Scargle cross-spectral peaks at $T = 24$, 12, 8, and 6 h, suggesting migrating tides, DW1, SW2, TW3, and QW4. Then, we arrange the cross-spectrum into a periodic table to batch spectral peaks of each expected Q2DW and all its potential SWs into one family. For each family, we estimate m through two approaches, the PDT on individual peaks and a family batched estimation. Consistent estimations of the approaches suggest two families, namely Q2DW3 with its five SWs, and Q2DW4 with its four SWs. These SWs entail tidal components DW1, SW2, TW3, and QW4, among which TW3 and QW4 are reported for the first time as the parent waves.

In the statistical study, cross-wavelet analysis is implemented to the wind observations between 2012 and 2019. The cross-wavelet spectra are composited into frequency-month depictions in three period ranges (near 2 days, 16 h, and 9.6 h), and altitude-month depictions at discrete frequencies. The near-2-day spectrum exhibits significant interannual variabilities and seasonal variation, which maximizes in July at $f = 0.57$–0.60, 0.48–0.50, and 0.50–0.55 cpd ($T = 40.0$–42.1, 48.0–50.0, and 48.0–43.6 h) associated with $m = 3$, 4, and -3, first two of which are R-G modes. The near-16-h and -9.6-h spectra maximize in local winter when the near-2-day spectra are weak locally, which we attribute speculatively to two potential factors, local modulation of tidal variation and potential SWs extended from the southern hemisphere, respectively. The Q2DWs and their SWs exhibit various altitude distributions. Given the potential relevance to global atmosphere-ionosphere coupling, the mechanisms underlying the height and seasonal-latitudinal behaviors of SWs revealed here warrant study by global models.

Data Availability Statement

The hourly wind data from Mohe is provided by the Data Center for Geophysics (http://www.dx.doi.org/10.12197/2020GA016), National Earth System Science Data Sharing Infrastructure at BNOSE (Beijing National Observatory of Space Environment), and IGGCAS (Institute of Geology and Geophysics, Chinese Academy of Sciences). The post-processed data used in the current paper are available at https://dx.doi.org/10.22000/353.

References

Alves, E. D. O., Lima, L. M., de Medeiros, A. F., Buriti, R. A., Batista, P. P., & Clemesha, B. R. (2013). Nonlinear interaction between diurnal tidal and 2-day wave in the meteor winds observed at cachoeira paulista-sp and Sao Joao do Cariri-PB, Brazil: A case study. *Revista Brasileira de Geofisica*, *31*(3), 403–412. https://doi.org/10.22564/rbgf.v31i3.313

Babadshanov, P. B., Kalchenko, B. V., Kashcheyev, B. L., & Fedynsky, V. V. (1973). Winds in the equatorial lower thermosphere. *Proceedings of the Academy of Sciences of the USSR*, 208, 1334–1337.

Beard, A. G., Mitchell, N. J. J., Williams, P. J. S. S. J. S., & Kunitake, M. (1999). Non-linear interactions between tides and planetary waves resulting in periodic tidal variability. *Journal of Atmospheric and Solar-Terrestrial Physics*, *61*(5), 363–376. https://doi.org/10.1016/S1364-6826(99)00003-6

Cevolani, G., & Kingsley, S. P. (1992). Non-linear effects on tidal and planetary waves in the lower thermosphere: Preliminary results. *Advances in Space Research*, *12*(10), 77–80. https://doi.org/10.1016/0273-1177(92)90446-5

Chau, J. L., & Clahsen, M. (2019). Empirical phase calibration for multistatic specular meteor radars using a beamforming approach. *Radio Science*, *54*, 60–71. https://doi.org/10.1029/2018RS006741

Forbes, J. M., & Moudden, Y. (2012). Quasi-two-day wave-tide interactions as revealed in satellite observations. *Journal of Geophysical Research*, *117*(12). https://doi.org/10.1029/2011JD017114

Gu, S. Y., Liu, H. L., Dou, X., & Jia, M. (2018). Ionospheric variability due to tides and quasi-two-day wave interactions. *Journal of Geophysical Research: Space Physics*, *123*(2), 1554–1565. https://doi.org/10.1002/2017JA025105

Gu, S. Y., Liu, H. L., Pedatella, N. M., Dou, X., & Liu, Y. (2017). On the wave number 2 eastward propagating quasi 2 day wave at middle and high latitudes. *Journal of Geophysical Research: Space Physics*, *122*(4), 4489–4499. https://doi.org/10.1002/2016JA023353

He, M., & Chau, J. L. (2019). Mesospheric semidiurnal tides and near-12 h waves through jointly analyzing observations of five specular meteor radars from three longitudinal sectors at boreal midlatitudes. *Atmospheric Chemistry and Physics*, *19*(9), 5993–6006. https://doi.org/10.5194/acp-19-5993-2019

He, M., Chau, J. L., Forbes, J. M., Thorsen, D., Li, G., Siddiqui, T. A., et al. (2020). Quasi-10-day wave and semidiurnal tide nonlinear interactions during the southern hemispheric SSW 2019 observed in the northern hemispheric mesosphere. *Geophysical Research Letters*, *47*(23), e2020GL091453. https://doi.org/10.1029/2020GL091453

He, M., Chau, J. L., Stober, G., Hall, C. M., Tsutsumi, M., & Hoffmann, P. (2017). Application of Manley-Rowe relation in analyzing nonlinear interactions between planetary waves and the solar semidiurnal tide during 2009 sudden stratospheric warming event. *Journal of Geophysical Research: Space Physics*, *122*(10), 10783–10795. https://doi.org/10.1002/2017JA024630

He, M., Chau, J. L., Stober, G., Li, G., Ning, B., & Hoffmann, P. (2018). Relations between semidiurnal tidal variants through diagnosing the zonal wavenumber using a phase differencing technique based on two ground-based detectors. *Journal of Geophysical Research: Atmospheres*, *123*(8), 4015–4026. https://doi.org/10.1002/2018JD028400

He, M., Forbes, J. M., Chau, J. L., Li, G., Wan, W., & Korotyshkin, D. V. (2020). High-order solar migrating tides quench at SSW onsets. *Geophysical Research Letters*, *47*(6), 1–8. https://doi.org/10.1029/2019GL086778

He, M., Liu, L., Wan, W., & Wei, Y. (2011). Strong evidence for couplings between the ionospheric wave-4 structure and atmospheric tides. *Geophysical Research Letters*, *38*(14). https://doi.org/10.1029/2011GL047855

Hocking, W. K., Fuller, B., & Vandepeer, B. (2001). Real-time determination of meteor-related parameters utilizing modern digital technology. *Journal of Atmospheric and Solar-Terrestrial Physics*, *63*(2), 155–169. https://doi.org/10.1016/S1364-6826(00)00138-3

Hoffmann, P., Becker, E., Singer, W., & Placke, M. (2010). Seasonal variation of mesospheric waves at northern middle and high latitudes. *Journal of Atmospheric and Solar-Terrestrial Physics*, *72*(14), 1068–1079. https://doi.org/10.1016/j.jastp.2010.07.002

Huang, K. M., Liu, A. Z., Lu, X., Li, Z., Gan, Q., Gong, Y., et al. (2013). Nonlinear coupling between quasi 2 day wave and tides based on meteor radar observations at Maui. *Journal of Geophysical Research: Atmospheres*, *118*(19), 10936–10943. https://doi.org/10.1002/jgrd.50872

Jacobi, C. (2012). 6 year mean prevailing winds and tides measured by VHF meteor radar over Collm (51.3N, 13.0E). *Journal of Atmospheric and Solar-Terrestrial Physics*, *78–79*, 8–18. https://doi.org/10.1016/j.jastp.2011.04.010

Lieberman, R. S., Riggin, D. M., Nguyen, V., Palo, S. E., Siskind, D. E., Mitchell, N. J., et al. (2017). Global observations of 2 day wave coupling to the diurnal tide in a high-altitude forecast-assimilation system. *Journal of Geophysical Research: Atmospheres*, *122*(8), 4135–4149. https://doi.org/10.1002/2016JD025144

Lilienthal, F., & Jacobi, C. (2015). Meteor radar quasi 2-day wave observations over 10 years at Collm (51.3N, 13.0E). *Atmospheric Chemistry and Physics*, *15*(17), 9917–9927. https://doi.org/10.5194/acp-15-9917-2015

Manson, A. H., Meek, C. E., Gregory, J. B., & Chakrabarty, D. K. (1982). Fluctuations in tidal (24-, 12-h) characteristics and oscillations (8-h-5-d) in the mesosphere and lower thermosphere (70–110 km): Saskatoon (52N, 107W), 1979–1981. *Planetary and Space Science*, *30*(12), 1283–1294. https://doi.org/10.1016/0032-0633(82)90102-7

Merzlyakov, E. G., Portnyagin, Y. I., Makarov, N. A., Forbes, J., & Palo, S. (2005). Eastward-propagating day-to-day wind oscillations in the northern polar mesosphere/lower thermosphere. *Izvestiya: Atmospheric and Oceanic Physics*, *41*(1), 80–92.

Moudden, Y., & Forbes, J. M. (2014). Quasi-two-day wave structure, interannual variability, and tidal interactions during the 2002–2011 decade. *Journal of Geophysical Research*, *119*(5), 2241–2260. https://doi.org/10.1002/2013JD020563

Muller, H. G. (1972). A discussion on D and E region winds over EuropeLong-period meteor wind oscillations. *Philosophical Transactions of the Royal Society of London – Series A: Mathematical, Physical and Engineering Sciences*, *271*(1217), 585–599. https://doi.org/10.1098/rsta.1972.0026

Nguyen, V. A., Palo, S. E., Lieberman, R. S., Forbes, J. M., Ortland, D. A., & Siskind, D. E. (2016). Generation of secondary waves arising from nonlinear interaction between the quasi 2-day wave and the migrating diurnal tide. *Journal of Geophysical Research: Atmospheres*, *121*(13), 7762–7780. https://doi.org/10.1002/2016JD024794

Palo, S. E., Roble, R. G., & Hagan, M. E. (1999). Middle atmosphere effects of the quasi-two-day wave determined from a general circulation model. *Earth, Planets and Space*, *51*(7–8), 629–647. https://doi.org/10.1186/BF03353221

Pancheva, D., Mukhtarov, P., & Siskind, D. E. (2018). The quasi-6-day waves in NOGAPS-ALPHA forecast model and their climatology in MLS/Aura measurements (2005–2014). *Journal of Atmospheric and Solar-Terrestrial Physics*, *181*, 19–37. https://doi.org/10.1016/j.jastp.2018.10.008

Pancheva, D., Mukhtarov, P., Siskind, D. E., & Smith, A. K. (2016). Global distribution and variability of quasi 2 day waves based on the NOGAPS-ALPHA reanalysis model. *Journal of Geophysical Research: Space Physics*, *121*(11), 11422–11449. https://doi.org/10.1002/2016JA023381

Pedatella, N. M., & Forbes, J. M. (2012). The quasi 2 day wave and spatial-temporal variability of the OH emission and ionosphere. *Journal of Geophysical Research*, *117*(1), 1–11. https://doi.org/10.1029/2011JA017186

Pfister, L. (1985). Baroclinic instability of easterly jets with applications to the summer mesosphere. *Journal of the Atmospheric Sciences*, *42*(4), 313–330. https://doi.org/10.1175/1520-0469(1985)042(0313:BIOEJW)2.0.CO;2

Plumb, R. A. (1983). Baroclinic instability of the summer mesosphere: a mechanism for the quasi-two-day wave? *Journal of the Atmospheric Sciences*, *40*(1), 262–270. https://doi.org/10.1175/1520-0469(1983)040(0262:BIOTSM)2.0.CO;2

Randel, W. J. (1994). Observations of the 2-Day wave in NMC stratospheric analyses. *Journal of the Atmospheric Sciences*, *51*(2), 306–313. https://doi.org/10.1175/1520-0469(1994)051(0306:OOTDWI)2.0.CO;2

Salby, M. L. (1981). Rossby normal modes in nonuniform background configurations. Part II. Equinox and solstice conditions. *Journal of the Atmospheric Sciences*, *38*(9), 1827–1840. https://doi.org/10.1175/1520-0469(1981)038(1827:RNMINB)2.0.CO;2

Salby, M. L., & Callaghan, P. F. (2001). Seasonal amplification of the 2-day wave: Relationship between normal mode and instability. *Journal of the Atmospheric Sciences*, *58*(14), 1858–1869. https://doi.org/10.1175/1520-0469(2001)058(1858:SAOTDW)2.0.CO;2

Salby, M. L., & Roper, R. G. (1980). Long-period oscillations in the meteor region. *Journal of the Atmospheric Sciences*, *37*(1), 237–244. https://doi.org/10.1175/1520-0469(1980)037(0237:LPOITM)2.0.CO;2

Sandford, D. J., Schwartz, M. J., & Mitchell, N. J. (2008). The wintertime two-day wave in the polar stratosphere, mesosphere and lower thermosphere. *Atmospheric Chemistry and Physics*, *8*(3), 749–755. https://doi.org/10.5194/acp-8-749-2008

Teitelbaum, H., & Vial, F. (1991). On tidal variability induced by nonlinear interaction with planetary waves. *Journal of Geophysical Research*, *96*(A8), 14169–14178. https://doi.org/10.1029/91ja01019

Teitelbaum, H., Vial, F., Manson, A. H., Giraldez, R., & Massebeuf, M. (1989). Non-linear interaction between the diurnal and semidiurnal tides: terdiurnal and diurnal secondary waves. *Journal of Atmospheric and Terrestrial Physics*, *51*(7), 627–634. https://doi.org/10.1016/0021-9169(89)90061-5

Torrence, C., & Compo, G. P. (1998). A practical guide to wavelet analysis. *Bulletin of the American Meteorological Society*, *79*(1), 61–78. https://doi.org/10.1175/1520-0477(1998)079(0061:APGTWA)2.0.CO;2

Tunbridge, V. M., Sandford, D. J., & Mitchell, N. J. (2011). Zonal wave numbers of the summertime 2 day planetary wave observed in the mesosphere by EOS Aura Microwave Limb Sounder. *Journal of Geophysical Research*, *116*(11), 1–16. https://doi.org/10.1029/2010JD014567

Yu, Y., Wan, W., Ning, B., Liu, L., Wang, Z., Hu, L., & Ren, Z. (2013). Tidal wind mapping from observations of a meteor radar chain in December 2011. *Journal of Geophysical Research: Space Physics*, *118*(5), 2321–2332. https://doi.org/10.1029/2012JA017976